Downloaded 06/25/21 to 174.52.196.181. Redistribution subject to SEG license or copyright; see Terms of Use at http://library.seg.org/page/policies/terms
DOI:10.1190/segam2020-3426801.1

Study of the Yellowstone crustal magmatic system with multiphysics data

Xiaolei TU[1] and Michael S. Zhdanov[1,2]; [1]University of Utah; [2]TechnoImaging*

Summary

Yellowstone volcanic field is characterized by hotspots, extensive earthquakes, ground deformation, and contains the world's largest concentration of hydrothermal features. Most of the previous geophysical studies in the Yellowstone area were based on separate inversions of different geophysical data, which suffered from inadequate data coverage, limited sensitivity, measurement errors, and nonuniqueness of the inverse problems. Joint inversion of multiphysics data is a practical approach to reduce the nonuniqueness and uncertainties in the inverse model parameters. This paper presents the results of joint inversion of the gravity and P-wave traveltimes data produced by local earthquakes in the Yellowstone area. We apply a novel joint inversion method based on Gramian constraints and multiscale resampling to image the crustal magmatic system of the Yellowstone. Our results have revealed a consistent L-shaped low-density and low-velocity anomaly just beneath the Yellowstone caldera.

Introduction

The Yellowstone volcanic field is located at the eastern end of the Snake River Plain, which was created as the North American Plate moved southwestward across a mantle plume (Schmandt et al., 2012; Huang et al., 2015). The Yellowstone volcanic field is characterized by hotspots, extensive earthquakes, ground deformation (Farrell et al., 2010; Huang et al., 2015), and contains approximately 50 percent of the world's hydrothermal features (Hurwitz and Lowenstern, 2014).

Global tomographic studies show that the youthful Yellowstone volcanic field is fed by a west-northwest-dipping plume that extends from the mid mantle to ~50 km depth (Yuan and Dueker, 2005; Smith et al., 2009; Schmandt et al., 2012; Porritt et al., 2014) which in turn provides basaltic magma that fuels the Yellowstone basaltic/rhyolitic crustal magma reservoir. Studies using local earthquake tomography reveal that the Yellowstone crustal magma reservoir extends well beyond the Yellowstone Caldera. A low-velocity body (LVB) consisting of P-wave velocity reduction as significant as 7% at a depth of 5 to 17 km was believed to have fueled the volcanism (Husen et al., 2004; Farrell et al., 2014). The shallowest portion of this upper-crustal magma body is responsible for the largest area of hydrothermal activity seen from the earth's surface in Yellowstone.

Due to a lack of adequate seismic stations and earthquakes in the key areas, tomography studies in the Yellowstone area suffered from limited resolution (Farrell et al., 2014), leading to increased uncertainty of the velocity models. The model uncertainty, however, could be reduced by incorporating additional constraints in the inversion. Joint inversion of multiphysics data applied constraint though complementing each dataset with information derived from other datasets (Zhdanov et al., 2012; Zhdanov, 2015). Different physical fields are sensitive to different properties and exhibit different sensitivity patterns as a result of their different governing physical laws. We could, therefore, harness the complementary sensitivities of them to produce geophysical models of the magmatic system with reduced uncertainty.

In order to image the Yellowstone crustal magmatic system, we jointly inverted the gravity data and P-wave first arrival traveltimes of local earthquakes recorded over 26 years from 1984 to 2011 in the Yellowstone area. Our joint inversion method is based on (1) a Gramian structural coupling term which enhances structural similarity between the density and velocity model; (2) a multiscale resampling strategy that honors the different resolution capabilities of the gravity field and seismic traveltimes; and (3) enforcing coupling of model parameters within those subdomains only where structural resemblance is present.

The results of joint inversion reveal an L-shaped low-density and low-velocity anomaly just beneath the Yellowstone caldera, which is consistent with previous studies in the same area. comparisons with previous studies

Joint inversion methodology

The joint regularized inversion of gravity and seismic traveltime data is performed by minimizing the following parametric functional (Zhdanov, et al., 2012; Zhdanov, 2015):

$$p=\sum_{i=1}^{2}\Phi^{(i)}\left(\mathbf{m}_s^{(i)}\right)+\sum_{i=1}^{2}\alpha^{(i)}\Psi^{(i)}\left(\mathbf{m}_s^{(i)}\right)+\beta s\left(\mathbf{m}_s^{(1)},\mathbf{m}_s^{(2)}\right), \quad (1)$$

where $\Phi^{(i)}$ denotes the misfit functional for the i-th type of data; $\Psi^{(i)}$ represents the stabilizer promoting preferred structures of the model; $s\left(\mathbf{m}_s^{(1)},\mathbf{m}_s^{(2)}\right)$ is the joint Gramian stabilizer enforcing structural coupling. Vectors $\mathbf{m}_s^{(1)}$ and $\mathbf{m}_s^{(2)}$ denote cubic B-spline subspace representation of the density and velocity model. Coefficients $\alpha^{(i)}$ and β are the regularization parameters balancing the misfits and the corresponding stabilizers.

One of the key features of the joint inversion method used in this project is an application of a multiscale resampling

© 2020 Society of Exploration Geophysicists

10.1190/segam2020-3426801.1

Downloaded 06/25/21 to 174.52.196.181. Redistribution subject to SEG license or copyright; see Terms of Use at http://library.seg.org/page/policies/terms
DOI:10.1190/segam2020-3426801.1

strategy, which honors different resolution capabilities of the gravity field and seismic traveltimes. The density and velocity models are assumed to be represented in a subspace of cubic B-spline functions. The density and velocity models are resampled by the coarse and fine meshes, respectively, to compute the gravity and seismic traveltime data. The models are resampled again in the same third mesh to facilitate the structural coupling between them. This mesh is coarser than or the same as density forward modeling mesh so that only the long-wavelength structures of the velocity model are preserved and matched with the density model.

We employ the robust norms for the misfit functional:

$$\Phi^{(i)}\left(\mathbf{m}_s^{(i)}\right) = \left\| \mathbf{W}_d^{(i)} \left[\mathbf{A}^{(i)} \left(\mathbf{L}_i \mathbf{m}_s^{(i)} \right) - \mathbf{d}^{(i)} \right] \right\|_\rho^2, \quad (2)$$

where $\mathbf{W}_d^{(i)}$ represents the corresponding data weighting matrix; $\mathbf{d}^{(i)}$ is the observed data, i.e., gravity data or P-wave first arrivals; $\| \ \|_\rho^2$ denotes the robust norm. $\mathbf{L}_i$ is the matrix of cubic B-spline functions resampling the model to the corresponding mesh. $\mathbf{A}^{(i)}$ denotes the forward operator for gravity field or seismic traveltimes. The gravity field is calculated with the point mass approximation method (Cuma et al., 2012). We use the multistage fast marching (FMM) method (De Kool et al., 2006; Rawlinson et al., 2006) to solve the isotropic eikonal equation for seismic traveltimes.

We could also incorporate a priori information into the inversion using the minimum norm (MN) stabilizer,

$$\Psi^{(i)}\left(\mathbf{m}_s^{(i)}\right) = \left\| \mathbf{W}_m^{(i)} \left(\mathbf{m}_s^{(i)} - \mathbf{m}_{apr}^{(i)} \right) \right\|^2, \quad (3)$$

which would favor the simplest model close to a prior model $\mathbf{m}_{apr}^{(i)}$. The model weights $\mathbf{W}_m^{(i)}$ in Eq. (3) and data weights $\mathbf{W}_d^{(i)}$ in Eq. (2) are determined based on the integrated sensitivity (Zhdanov, 2015), to provide an equal sensitivity of the different components of observed data to the cells located at different depths and horizontal positions.

Another new development of our joint inversion method is the Gramian based structural coupling term which could promote structural resemblance between velocity perturbation and density:

$$s\left(\mathbf{m}_s^{(1)}, \mathbf{m}_s^{(2)}\right) = \iiint_{\boldsymbol{D}} w_p^2 g\left(\boldsymbol{\nabla}\left(\mathbf{T}^{(1)} \mathbf{L}_3 \mathbf{m}_s^{(1)}\right), \boldsymbol{\nabla}\left(\mathbf{T}^{(2)} \mathbf{L}_3 \mathbf{m}_s^{(2)}\right) \right) dv, \quad (4)$$

where $w_p(\mathbf{r})$ is the probability of existing the model structural similarity at point $\mathbf{r}$; D is the inversion domain; $\boldsymbol{\nabla} = \left[\nabla_x, \nabla_y, \nabla_z\right]^T$ denotes the gradient operator. Operators $\mathbf{T}^{(1)}$ and $\mathbf{T}^{(2)}$ transform the models into some other model parameter space. The matrix of cubic B-spline basis, $\mathbf{L_3}$, resamples the models with the same coarse mesh so that the two models are coupled at the same scale. Function $g(,)$ represents the Gramian (i.e., the determinant of the Gram matrix) of the gradient at a given point.

We solve the minimization problem (1) with the re-weighted regularized conjugate gradient method (RRCG) (Zhdanov, 2015).

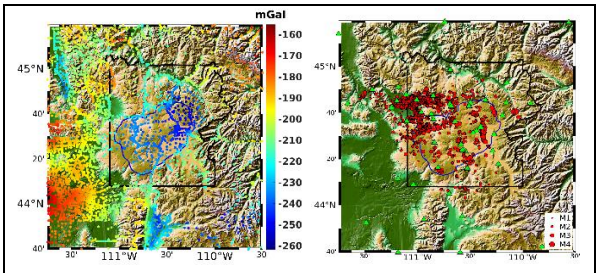

Figure 1: Map of Yellowstone National Park. Black solid lines denote the border of Yellowstone National Park. The Late Quaternary Yellowstone caldera was outlined in blue. (Left) dots represent the gravity stations with color of the stations scaled by their values of complete Bouguer anomaly. (right) Seismic stations and earthquakes are denoted by green triangles and red dots, respectively. The area of the red dots represents the magnitude of the earthquakes.

Yellowstone data

The gravity data used in this study were acquired by the United States Geological Survey (USGS), the University of Utah, and the Pan American Center for Earth and Environmental Sciences (PACES). Figure 1 presents a map of the gravity station distributions and the complete Bouguer anomaly. The data have been previously modeled by DeNosaquo et al. (2009). They suggested a low density ($\sim 2.52\ g/cm^3$) anomaly beneath the caldera at a depth of $10\ km$ to $20\ km$. Jorgensen and Zhdanov (2019) jointly inverted the same gravity data with magnetotelluric data and inferred partial melt in both upper and lower crust. However, the density models in those studies are of limited resolution and considerable uncertainty, caused by insufficient gravity station coverage, especially in the east of the survey area, and by non-uniqueness of the gravity inverse problem. Additional constraints could be introduced by jointly inverting the data with seismic traveltime data.

We employ a record of 26 years earthquakes in the key areas of Yellowstone from 1984 to 2011 to derive a data set of consistently picked P phase first arrival times. To ensure that only the highest-quality data were used for the inversion, we considered earthquakes that had at least eight P-wave observations, an azimuthal gap of less than 180°, and picks with arrival time uncertainties of less than $0.12\ s$. The final P phase data set consisted of 48,622 high-quality first arrivals from 4520 earthquakes. Figure 1 is a map of the

© 2020 Society of Exploration Geophysicists

Downloaded 06/25/21 to 174.52.196.181. Redistribution subject to SEG license or copyright; see Terms of Use at http://library.seg.org/page/policies/terms
DOI:10.1190/segam2020-3426801.1

Yellowstone volcanic field showing the topography. The red dots in Figure 1 denote the earthquakes selected in this study.

Inversion results

A. Inversion setup

The density and velocity models are represented in the same cubic B-splines subspace, and are resampled with meshes of different scales for forward modeling and structural coupling in the joint inversion. Table 1 presents the setup of knots and meshes for Yellowstone data. The decoupled forward modeling meshes would, therefore, honor the resolution capabilities of both gravity and seismic data. In the structural coupling stage of the joint inversion, the density and velocity models are again resampled with a coarse mesh. Consequently, only long-wavelength (i.e., $\geq 4\,km$) structures of density and velocity models are enforced to resemble each other. Small (i.e., $< 4\,km$) anomalies beyond the resolution capability of gravity data would not be artificially introduced to the gravity model but could still be preserved in the velocity model.

Table 1: Inversion setup with multiscale resampling

Knot/mesh	Interval/cell size Long. × Lat. × Depth	Num. of knots/Cells Long. × Lat. × Depth
Subspace representation	$0.1^{\circ} \times 0.1^{\circ} \times$ 3 km	27 × 23 × 12
Density: forward modeling	$0.04^{\circ} \times 0.04^{\circ} \times$ 2 km	61 × 51 × 14
Velocity: forward modeling	$0.1^{\circ} \times 0.1^{\circ} \times$ 3 km	233 × 201 × 28
Structural coupling	$0.04^{\circ} \times 0.04^{\circ} \times$ 2 km	61 × 51 × 14

The separate and joint inversions are terminated at the same threshold of the misfits. The thresholds of relative misfits for gravity and seismic traveltime data are 7% and 40%, respectively, which correspond to the weighted data root-mean-square misfits of 1.95 $mGal$ and 0.12 s.

B. Sensitivity analysis

Sensitivity analysis is a necessary tool to quantify the reliability of the inverted models. Any geophysical survey may have limited sensitivity to some sections of the examined subsurface area (Zhdanov, 2015), due to factors such as data coverage, survey configuration, and physical laws governing the geophysical fields. Joint inversion of multiphysics data reduces the model uncertainty by complementing the sensitivity of one physical property with others. The usage of complementary sensitivities should enhance the qualities of the inverted models. We calculate the integrated sensitivities of the Yellowstone gravity and seismic traveltimes in the subspace with the following formulas (Zhdanov, 2015):

$$\mathbf{S}^{(i)} = \frac{\left\|\delta \mathbf{d}^{(i)}\right\|}{\delta \mathbf{m}_s^{(i)}} = \sqrt{\mathbf{L}_i^T \mathbf{F}^{(i)^T} \mathbf{F}^{(i)} \mathbf{L}_i}\,, i = 1,2; \qquad (5)$$

where T denotes the matrix transpose operator; $\mathbf{F}^{(i)}$ represents the Fréchet matrix of the forward operator for density or P-wave velocity. The integrated sensitivity provides a measurement of the data sensitivity for every subsurface position.

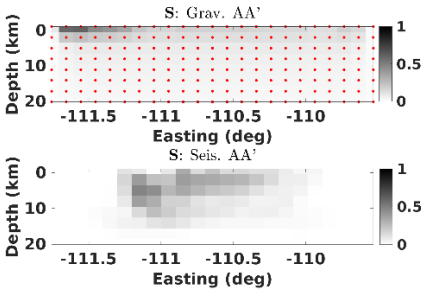

Figure 2: Vertical sections of normalized integrated sensitivity of gravity field (top) and seismic traveltimes (bottom) across section AA'. The red dots show vertical location of the knots for subspace representation.

Figure 2 presents vertical sections of the integrated sensitivity. The gravity sensitivity presents a horizontally uniform pattern. The distribution of seismic sensitivity is, comparatively, very sparse. The seismic data have only sufficient sensitivity in the Yellowstone Caldera and nearby areas, leaving vast areas outside the Yellowstone National Park under resolved. This problem could be mitigated by additional constraints from gravity data through joint inversion of seismic and gravity data. Besides, the gravity sensitivity decreases rapidly with depth, making it hard to recover the deep density anomaly. The seismic data complement the limited sensitivity of the gravity field at depth, constraining the depth of the density anomaly.

C. Results and discussion

We first applied separate gravity and seismic tomographic inversions to the data and then jointly inverted them. Horizontal sections of the inverted models at a depth of 8.7 km are presented in Figure 3. The patterns in separate and jointly inverted models are consistent for both density and velocity, as further confirmed by a vertical profile AA' in Figure 4. However, the depth of the density anomaly is better constrained in the jointly inverted model. The density and velocity models obtained with joint inversion present a consistent anomaly in the caldera area.

Figure 6 presents a comparison of the jointly inverted density and velocity models with published results (Jorgensen and Zhdanov, 2019; Huang et al., 2015). The pattern of the shallow anomaly is consistent for all models. Jorgensen and Zhdanov's density model, however, resolves a deeper anomaly below 20 km since their model was constrained by a deep conductivity model from

© 2020 Society of Exploration Geophysicists

Downloaded 06/25/21 to 174.52.196.181. Redistribution subject to SEG license or copyright; see Terms of Use at http://library.seg.org/page/policies/terms
DOI:10.1190/segam2020-3426801.1

magnetotelluric data. Huang's velocity model also presents a deep velocity low anomaly constrained by teleseismic data.

The data fitting for the gravity field is presented in Figure 7. The separately and jointly inverted density models predict the gravity data equally well, with a relative misfit of 7%. We also calculated the averaged traveltime residuals for each seismic station, as illustrated in Figure 8. The data again are fitted equally well to the noise level.

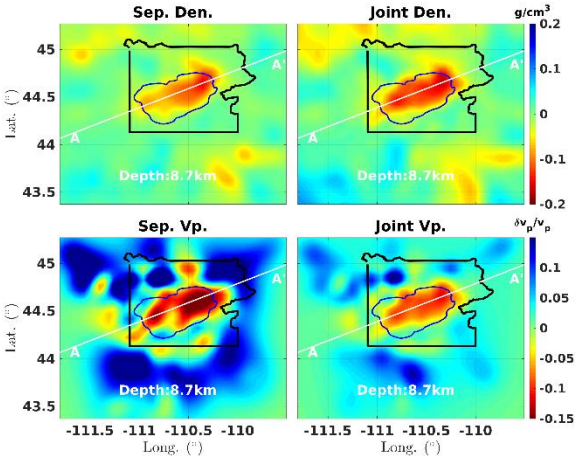

Figure 3: Horizontal sections of separately and jointly inverted density and velocity models at the depth of 8.7 km below sea level.

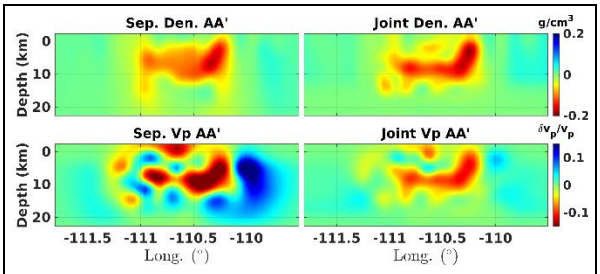

Figure 5: Vertical profile AA' of the separately and jointly inverted density and velocity models. The corresponding location of the profile is marked by solid white line on the horizontal sections.

Conclusions

The developed method of joint inversion of multiphysics data enhances the structural similarity between model parameters and honors the resolution differences of different geophysical methods. We have applied the developed method to the geophysical data collected over the Yellowstone area and jointly inverted the gravity data and P-wave traveltimes of local earthquakes to image the crustal magmatic system. Our results have revealed a consistent L-shaped low-density and low-velocity anomaly just beneath the Yellowstone caldera, which is consistent with previous studies in the same area.

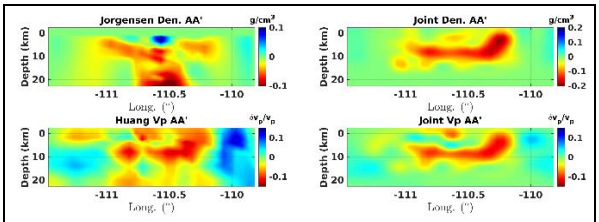

Figure 6: Comparision of joint inverted models with published results of profile AA'. Note the different density colorbars.

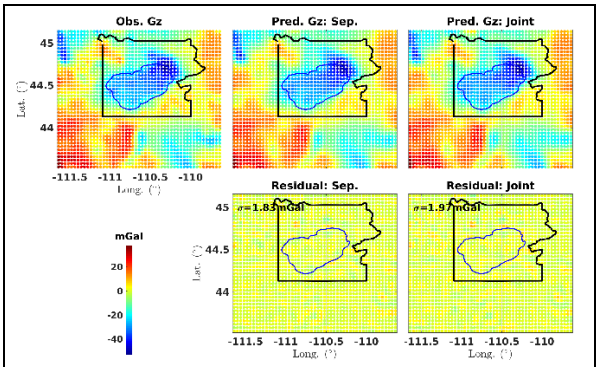

Figure 7: Maps of gravity data fitting for separate and joint inversions. Both separate and joint inversions are converged to a relative data misfit of 7%.

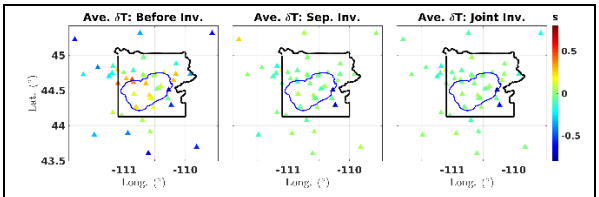

Figure 8: Averaged traveltime residuals at each seismic station before (left), and after separate (middle) and joint (right) inversions. Both separate and joint inversions are converged to a relative data misfit of 40%, i.e., 60% residual reduction. The residuals of the YPLB and YTC_ station didn't change much before and after the inversions.

Acknowledgments

We are thankful to the Consortium for Electromagnetic Modeling and Inversion, University of Utah, and TechnoImaging for supporting this research. We also thank the University of Utah Seismograph Stations and USGS for providing the earthquake seismic and gravity data.

© 2020 Society of Exploration Geophysicists

REFERENCES

Čuma, M., G. A. Wilson, and M. S. Zhdanov, 2012, Large scale 3D inversion of potential field data: Geophysical Prospecting, **60**, 1186–1199, doi: https://doi.org/10.1111/j.1365-2478.2011.01052.x.

de Kool, M., N. Rawlinson, and M. Sambridge, 2006, A practical grid-based method for tracking multiple refraction and reflection phases in three-dimensional heterogeneous media: Geophysical Journal International, **167**, 253–270, doi: https://doi.org/10.1111/j.1365-246X.2006.03078.x.

DeNosaquo, K. R., R. B. Smith, and A. R. Lowry, 2009, Density and lithospheric strength models of the Yellowstone–Snake River Plain volcanic system from gravity and heat flow data: Journal of Volcanology and Geothermal Research, **188**, 108–127, doi: https://doi.org/10.1016/j.jvolgeores.2009.08.006.

Farrell, J., R. B. Smith, S. Husen, and T. Diehl, 2014, Tomography from 26 years of seismicity revealing that the spatial extent of the Yellowstone crustal magma reservoir extends well beyond the Yellowstone caldera: Geophysical Research Letters, **41**, 3068–3073, doi: https://doi.org/10.1002/2014GL059588.

Huang, H.-H., F.-C. Lin, B. Schmandt, J. Farrell, R. B. Smith, and V. C. Tsai, 2015, The Yellowstone magmatic system from the mantle plume to the upper crust: Science, **348**, 773–776, doi: https://doi.org/10.1126/science.aaa5648.

Hurwitz, S., and J. B. Lowenstern, 2014, Dynamics of the Yellowstone hydrothermal system: Reviews of Geophysics, **52**, 375–411, doi: https://doi.org/10.1002/2014RG000452.

Husen, S., R. B. Smith, and G. P. Waite, 2004, Evidence for gas and magmatic sources beneath the Yellowstone volcanic field from seismic tomographic imaging: Journal of Volcanology and Geothermal Research, **131**, 397–410, doi: https://doi.org/10.1016/S0377-0273(03)00416-5.

Jorgensen, M., and M. S. Zhdanov, 2019, Imaging Yellowstone magmatic system by the joint Gramian inversion of gravity and magnetotelluric data: Physics of the Earth and Planetary Interiors, **292**, 12–20, doi: https://doi.org/10.1016/j.pepi.2019.05.003.

Porritt, R. W., R. M. Allen, and F. F. Pollitz, 2014, Seismic imaging east of the Rocky Mountains with USArray: Earth and Planetary Science Letters, **402**, 16–25, doi: https://doi.org/10.1016/j.epsl.2013.10.034.

Rawlinson, N., and M. Sambridge, 2004, Wave front evolution in strongly heterogeneous layered media using the fast marching method: Geophysical Journal International, **156**, 631–647, doi: https://doi.org/10.1111/j.1365-246X.2004.02153.x.

Schmandt, B., K. Dueker, E. Humphreys, and S. Hansen, 2012, Hot mantle upwelling across the 660 beneath Yellowstone: Earth and Planetary Science Letters, **331-332**, 224–236, doi: https://doi.org/10.1016/j.epsl.2012.03.025.

Smith, R. B., M. Jordan, B. Steinberger, C. M. Puskas, J. Farrell, G. P. Waite, S. Husen, W.-L. Chang, and R. O'Connell, 2009, Geodynamics of the Yellowstone hotspot and mantle plume: Seismic and GPS imaging, kinematics, and mantle flow: Journal of Volcanology and Geothermal Research, **188**, 26–56, doi: https://doi.org/10.1016/j.jvolgeores.2009.08.020.

Yuan, H., and K. Dueker, 2005, Teleseismic P-wave tomogram of the Yellowstone plume: Geophysical Research Letters, **32**, doi: https://doi.org/10.1029/2004GL022056.

Zhdanov, M. S., 2015, Inverse theory and applications in geophysics, 2nd ed.: Elsevier.

Zhdanov, M. S., A. Gribenko, and G. Wilson, 2012, Generalized joint inversion of multimodal geophysical data using Gramian constraints: Geophysical Research Letters, **39**, doi: https://doi.org/10.1029/2012GL051233.

Downloaded 06/25/21 to 174.52.196.181. Redistribution subject to SEG license or copyright; see Terms of Use at http://library.seg.org/page/policies/terms
DOI:10.1190/segam2020-3426801.1